Title

Microarchitectural Changes of Cardiovascular Calcification in Response to In Vivo Interventions Using Deep-Learning Segmentation and Computed Tomography Radiomics.

Journal

Arteriosclerosis, Thrombosis and Vascular Biology, 42(8)

Authors

Patel, Nikhil
Setya, Kulveer
Pradhan, Stuti
et al.

Publication Date

2022-08-01

DOI

10.1161/ATVBAHA.122.317761

Peer reviewed

HHS Public Access

Author manuscript

Arterioscler Thromb Vasc Biol. Author manuscript; available in PMC 2023 August 01.

Published in final edited form as:

Arterioscler Thromb Vasc Biol. 2022 August ; 42(8): e228–e241. doi:10.1161/ATVBAHA.122.317761.

Microarchitectural Changes of Cardiovascular Calcification in Response to In Vivo Interventions Using Deep Learning Segmentation and CT Radiomics

NR Patel[1], **K Setya**[1], **S Pradhan**[1], **M Lu**[1], **LL Demer**[1,2,3,5], **Y Tintut**[1,3,4,5]

[1]Department of Medicine, University of California, Los Angeles (UCLA), Los Angeles, CA 90095-1679

[2]Department of Bioengineering, University of California, Los Angeles (UCLA), Los Angeles, CA 90095-1679

[3]Department of Physiology, University of California, Los Angeles (UCLA), Los Angeles, CA 90095-1679

[4]Department of Orthopaedic Surgery, University of California, Los Angeles (UCLA), Los Angeles, CA 90095-1679

[5]VA Greater Los Angeles Healthcare System, Los Angeles, CA 90073-1003

Abstract

Background: Coronary calcification associates closely with cardiovascular risk, but its progress is accelerated in response to some interventions widely used to reduce risk. This paradox suggests that qualitative, not just quantitative, changes in calcification may affect plaque stability. To determine if the microarchitecture of calcification varies with aging, Western diet, statin therapy, and high intensity, progressive exercise, we assessed changes in a priori selected CT radiomic features (intensity, size, shape, and texture).

Methods: Longitudinal CT scans of mice (*Apoe*$^{-/-}$) exposed to each of these conditions were auto-segmented by deep learning segmentation, and radiomic features of the largest deposits were analyzed.

Results: Over 20 weeks of aging, intensity and most size parameters increased, but surface-area-to-volume ratio (a measure of porosity) decreased, suggesting stabilization. However, texture features (coarseness, cluster tendency and non-uniformity) increased, suggesting heterogeneity and likely destabilization. Shape parameters showed no significant changes, except sphericity, which showed a decrease. The Western diet had significant effects on radiomic features related to size and texture, but not intensity or shape. In mice undergoing either pravastatin treatment or exercise, the selected radiomic features of their CT scans were not significantly different from those of their respective controls. Interestingly, the total number of calcific deposits increased

Address for correspondence: Yin Tintut, PhD, University of California, Los Angeles, 10833 Le Conte Avenue, Los Angeles, CA 90095-1679, ytintut@mednet.ucla.edu, 310-206-9964.

Disclosure: None

significantly less in the two intervention groups compared with the respective controls, suggesting more coalescence and/or fewer de novo deposits.

Conclusions: Thus, aging and standard interventions alter the microarchitectural features of vascular calcium deposits in ways that may alter plaque biomechanical stability.

Graphical Abstract

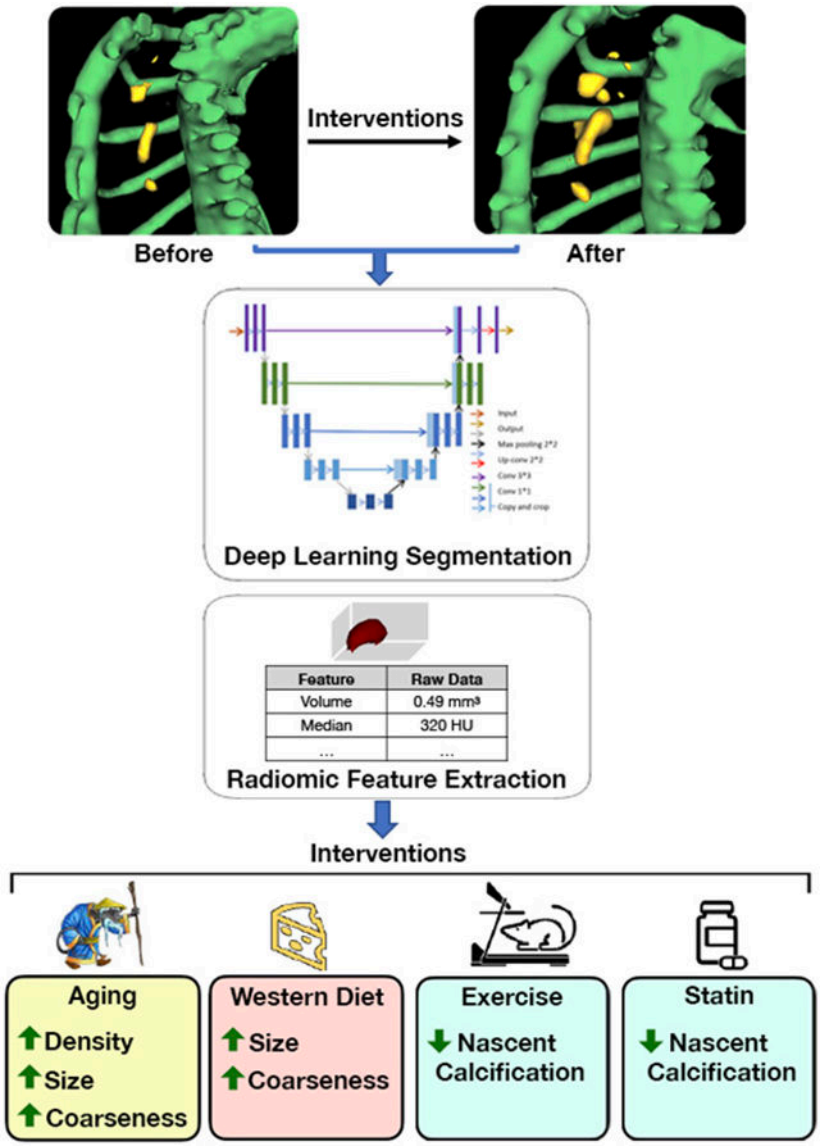

Keywords

Calcification; cardiovascular; CT; radiomics; aging; atherosclerosis; exercise; hyperlipidemia

INTRODUCTION

The degree of coronary artery calcification correlates with a greater atherosclerotic plaque burden [1], atherosclerotic plaque instability [2], and the risk of myocardial infarction [3]. It is hypothesized to modulate clinical risk by increasing risk of atherosclerotic plaque rupture. Clinically, coronary calcification is measured as calcium mineral content or “calcium score” based on x-ray attenuation in various types of computed tomographic (CT) imaging that reduce or freeze the motion of the heart. However, recent studies suggest that a more nuanced evaluation of the calcium deposits is warranted. For instance, the Multi-Ethnic Study of Atherosclerosis found that adverse cardiovascular events correlated more closely to a rough estimate of calcium mineral density than to calcium content [4]. Recent studies also raise the question of whether multiple small deposits confer greater risk than single large deposits of the same volume [5]. Due to the pulsatile nature of blood pressure, the artery wall is subject to significant oscillatory solid mechanical stresses in both circumferential and longitudinal axes, exposing calcium deposits to compliance mismatch at the interface between the rigid mineral surface and the distensible vascular tissues surrounding it [6]. Such conditions are known to cause de-bonding, in which the deposit separates from the surrounding tissue at the surface facing the direction of stress but not at the surface facing compressive stress [7] where rupture stress is reduced. These findings suggest that the surface area of calcium deposits may increase risk of debonding and rupture.

The progression of vascular calcification is a hallmark of aging [8]. It also progresses with high-fat diets, and, unexpectedly, even with certain pharmacological and non-pharmacological interventions that reduce risk. Although statins lower cholesterol levels, slow atherosclerotic progression, and lower cardiovascular risk, they are now known to increase the calcium content of coronary arteries [9, 10]. Similarly, elite athletes, who have, in general, a lower risk of coronary artery disease and higher life expectancy [11, 12], have a greater prevalence of coronary calcification and higher calcium scores by CT [13]. These findings suggest that a secondary mechanism may be at play in reducing plaque rupture risk. One possibility is a risk-altering change in morphological or microarchitectural features of the calcium deposits [5, 14]. The size, shape, and texture of mineral deposits may be critical determinants of their biomechanical features and plaque stability, features that cannot be determined from CT-derived calcium scores alone.

Algorithms for analyzing CT images have evolved substantially in recent years, but coronary calcium scans still use a decades-old, clinical “calcium score,” which has serious limitations due to truncation, smoothing, and voxelation of raw density values imposed by a crude algorithm known as the Agatston method [15]. Based on a rough estimate of density derived retrospectively from Agatston scores, Criqui and colleagues raise a question of whether the density of calcium deposits may have more predictive value than the calcium scores, where density relates inversely with cardiovascular risk [4, 16]. This is consistent with the expected inverse association of density with surface area. Cahalane and colleagues analyzed human CT data and tissue nanoindentation testing and also found that radiographic density had a strong positive correlation with both elastic modulus and hardness of the tissue samples [17]. Thus, analyzing differences in density of calcific lesions may provide insight into the mechanical attributes that dictate plaque stability.

In CT scans, density is proportional to X-ray attenuation, which is used to produce an image consisting of gray levels. Denser tissue has greater x-ray attenuation, measured in Hounsfield units (HU), and it is shown as brightness on images with positive values on quantitation; thus, “intensity” on CT images corresponds positively with tissue density. These gray levels provide data suitable for radiomic analysis. Radiomics, the extraction of minable imaging features from radiological images, allows for the quantification of previously unexplored features such as “texture” that have been valuable in the diagnosis of tumors and prognosis in oncology. In clinical cardiac CT, addition of a quantitative score based on radiomic features to the conventional Agatston calcium scores significantly improved the predictive value in a 9-year follow-up of the Offspring and Third Generation cohorts of the community-based Framingham Heart Study [18]. Thus, radiomic analysis may improve interpretation of the significance of calcium deposits on cardiac CT.

A necessary first step in calculating radiomic features is the CT segmentation of calcium deposits, defining and detecting the edges of deposits based on a threshold of x-ray attenuation. Manual segmentation is a tedious and time-consuming task that is highly susceptible to subjective influence [19, 20]. In contrast, deep learning segmentation, trained on blinded manual segmentation, greatly reduces variability, in that edges are defined solely based on objective image features learned by the algorithm [20]. Deep learning algorithms also achieve accurate anatomical segmentations automatically in multiple imaging modalities [21].

In the present study, we examined the effects of aging, Western diet, statin treatment, and high intensity, progressive exercise on the morphology of vascular calcification in a murine model of calcific atherosclerosis using computational image processing and deep learning networks in a longitudinal study of serial, in vivo micro-computed tomographic imaging.

METHODS

The authors declare that all supporting data are available within the article [and its online supplementary files].

Datasets used for analysis

Datasets included CT images of cardiovascular calcification from our prior studies of mice (female, *Apoe*$^{-/-}$) subjected to various treatment regimens [22, 23]. The first study consisted of mice on a Western diet (21% fat and 0.2% total cholesterol by weight; TD88137, Envigo) subjected to either control activity (ad lib) or a high-intensity, progressive exercise regimen over the course of 9 weeks, and CT scans of each mouse were taken at the beginning and end of this 9-week interval [22]. The second study consisted of mice on a standard diet subjected to either control or pravastatin for a course of 20 weeks [23]. CT scans of each mouse for the pravastatin study were obtained at three individual time points: Pre (0 weeks), Mid (10 weeks), and Post (20 weeks) treatment. Of note, although CT scans were acquired at 3 different time-points for both control and statin groups, only the first and the last time-points were used in the statin analysis to focus on the maximal change (based on the prior findings that calcification progression is monotonic). The middle time-point scans

of the untreated mice were used as controls for the Western diet analysis to match the diet duration.

Manual segmentation of calcification

To obtain data to train a deep learning segmentation algorithm, careful slice-by-slice segmentation of aortic calcification on murine CT scans was completed using a specialized software, three-dimensional (3-D) Slicer (v. 4.10.2). CT scans (n = 111) were segmented, providing 2-D images (103,008 total) for training use. Two different operators completed these segmentations to account for inter-operator variability and both were blinded to intervention groups. To provide more data for training, we employed a 90:10 train-test split, which provided 92,707 images for training and 10,301 images for testing. These manual segmentations serve as the dataset for the segmentation algorithm training as well as a comparison marker to verify any morphological insights obtained from the algorithm. The manual segmentations were only used for algorithmic training and were not subsequently used for analysis or conclusions.

U-Net segmentation training

For automated segmentation, we used a specialized deep learning model architecture, U-Net, that has become increasingly popular due to its high performance in precise image segmentation while training on relatively few images (arXiv:1505.04597). We utilized a modified approach to the original U-Net, as proposed by Ronneberger et al 2015 [24], using the Python package, Keras, to extend the segmentation architecture into 3 dimensions. Volumetric CT data was sliced in the transverse plane to produce 928 two-dimensional images per subject of size 384 x 384 pixels for each scan. The images were then normalized by the mean and standard deviations of their HU intensity values. To avoid correlation between the training and testing datasets, all 928 images for a given mouse subject were restricted to either the training or testing datasets. In addition, to provide the U-Net algorithm with greater contextualization of the 2-D image within the volumetric scan, the previous and following images that were adjacent in the z-axis were introduced as separate channels and fed simultaneously during learning.

After numerous trials with different learning rates, the optimal rate was determined to be 10^{-5} using Adam, an adaptive learning rate optimization algorithm, as the optimizer. Because of the severe class imbalance within the dataset (i.e., calcification-positive voxels made up less than 1% of each scan), the algorithm resolved to learn to output blank masks at first. Using the Sørensen-Dice coefficient, a statistic that gauges the pixel-wise similarity between two images, as the loss function initially helped to resolve the intra-image class imbalance. The imbalance in calcification-positive and calcification-negative images that were fed into the network was addressed by including all the calcification positive images and then randomly including an equal number of calcification negative images from the rest of the dataset.

Radiomic feature extraction

PyRadiomics, an open-source Python package for extracting radiomic features from 3-D volumetric images [25], was chosen for morphological multislice feature extraction because

it calculates radiomic values for each segmentation. Since radiomic features are generated for one calcium deposit at a time, the largest calcific deposit in each mouse was selected for comparisons; we posited that the largest deposit is most likely to be representative of the microarchitecture for each subject [26]. In addition, to ensure that the progression over time was assessed correctly, we checked a random sample of 5% of the scans; in every case, the largest deposit on the first (Pre) scan was the same as the largest deposit on the final (Post) scan. Specific features were selected for analysis *a priori* on biological basis, including intensity, size, shape, and texture. ***Intensity*** features included the first order statistics calculated from the histogram of all calcification voxel intensities, including the 10^{th} percentile, Median, and 90^{th} percentile of the gray level intensity within the region of interest. ***Size*** features included surface area (SA), volume (V), maximum 3-D diameter, and surface-area-to-volume ratio (SA/V). Maximum 3-D diameter is defined by PyRadiomics as the largest pairwise Euclidean distance between two points in the calcium deposits. ***Shape*** features included elongation, flatness, and sphericity. Elongation, in this algorithm, is defined in a manner opposite to its general meaning, as the square root of the ratio of the smaller to the larger of the two largest principal component axes (two orthogonal axes) in the calcium deposits. Flatness similarly indicates the relationship between the largest and smallest principal component axes in a manner opposite to the general meaning. Sphericity is a measure from 0 to 1 that quantifies the roundness of a calcium deposit relative to a sphere, where a value of 1 indicates a perfect sphere. ***Texture*** features included autocorrelation (a measure of the magnitude of the fineness and coarseness of the image texture from the 3-D gray level co-occurrence matrix) and cluster tendency (a measure of groupings of voxels with similar gray level values from the 3-D gray level co-occurrence matrix), and non-uniformity (a measure of the variability of gray level from the 3-D gray level run-length matrix). Notably, the term cluster tendency does not refer to clustering of individual deposits, rather it refers to variations in voxel intensities within the single deposit of interest. For each feature, the multiple 2-D CT slices of each largest deposit (for each mouse at each time point) were processed by deep learning segmentation (to identify calcium deposits) and then reconstructed into single 3-D images for analysis and quantitation of the radiomic features, using PyRadiomics, which processes volumetric data rather than 2-D images. The equations used by PyRadiomics to calculate these features from the voxel locations and intensities of the calcification ROI are included in Table I. All the radiomic features are included in Supplemental Tables I-IV.

Enumeration of spatially isolated deposits

The numbers of spatially isolated, calcified deposits were determined using the *morphology.label* algorithm from the Python package *scikit-learn*, which labels regions of an integer array that are connected by 2 or fewer orthogonal hops. Spatially isolated was defined as not having any adjacent voxels in common between two deposits. The results of this algorithm were additionally validated by counting the number of deposits in a visual examination of the 3-D reconstructed images of the thoracic cage in the *3-D slicer* program *(v. 4.10.2)* (https://www.slicer.org).

Histology and alizarin red staining

For histological analysis, we combined aortic root sections of *Apoe*$^{-/-}$ mice from prior studies [23, 26]. At euthanasia, mouse aortic roots were cryo-sectioned (10 μm thick), stained with Alizarin red to identify calcification, and imaged by light microscopy. Histological images were processed using ImageJ (*v.* 1.53) and analyzed using a custom MATLAB program that acquired the cross-sectional area (CSA) and perimeter of each calcium deposit.

Statistical analyses

Statistical analyses were performed using *GraphPad PRISM v. 9.1.0*. Normality of the data was first assessed, and equal variance was tested for parametric data. For comparisons between two groups, Student's *t*-test (two-tailed, paired, where appropriate) was used when data distributions for both groups were parametric (normally distributed) and had equal variances; otherwise, a *t*-test with Welch's correction was used. For comparisons of the non-parametric data between two groups, Mann-Whitney test was used. A paired *t*-test was used for comparison of data of the same mouse between different time points. For comparisons among multiple groups with repeated measures, two-way ANOVA followed by Holm-Sidak post-hoc analysis was employed. A p-value ≤ 0.05 was considered statistically significant.

RESULTS

Implementation of deep learning segmentation

We first implemented the deep learning segmentation algorithm to automatically segment the CT images (Fig. 1). We randomly chose 90% of the CT dataset from our prior studies in mice [22, 23] to manually segment and slice in the transverse plane to create 2-D images to feed into a modified U-Net Deep Learning model for training. The remaining 10% of the CT dataset was saved for testing of the algorithm. After completion of training and testing, the U-Net Deep Learning model was validated by assessing the Dice coefficient, which measures overlap between U-Net auto vs. manual segmentation, where a perfect match has a value of 1. The Dice coefficient was determined to be 0.89, indicating good accuracy of the automatic segmentation. The 11% non-overlap between the automatic and manual segmentations may be due to the variability in the manual delineation of calcification boundaries with soft (non-crisp) edges, as shown in Fig. 2.

Effects of aging on morphological progression of vascular calcium deposits

Using the finalized U-Net segmentation algorithm, we followed the morphological progression of vascular calcification that occurred in each mouse over 20 weeks of aging, from 55-week-old (55 wo) to 75 wo (Group A; Fig. 3A). Fig. 4 shows an example of the images used in the radiomic feature analysis of the largest deposit in each mouse, whereas Table II lists the radiomic features averaged over all the mice. The intensity features (10^{th} Percentile, Median, and 90^{th} Percentile of voxel intensities) increased significantly (1.05-fold, 1.11-fold, 1.25-fold, respectively). As for the size features, surface area, volume, and max 3-D diameter increased significantly (1.73-fold, 1.98-fold, 1.36-fold, respectively).

The SA/V ratio was decreased (0.82-fold) after 20 weeks of aging, suggesting a reduction of porosity (to use cardiovascular terms, reduced trabeculation or increased compaction), possibly through a “filling in” of gaps with new mineral. With respect to shape features, elongation and flatness did not change with aging. However, sphericity decreased (0.94-fold), suggesting that the shape of the deposit was less round. As for texture features, autocorrelation (coarseness), cluster tendency, and non-uniformity increased significantly (1.76-fold, 3.97-fold, 1.56-fold, respectively), suggesting coarseness and heterogeneity of the deposits also increased with age.

To further assess the *age-related rate* of morphological changes of the largest deposits, we compared changes in radiomic parameters over two 10-week age intervals [starting from age 55 weeks vs. starting from 65 weeks (Group A, Mid to Pre vs. Post to Mid; Fig. 3B)]. Results showed that the radiomic features showed no significant differences between the age intervals (data not shown), except for the 10^{th} percentile intensity, which showed an increase in almost all the deposits over the earlier age interval (Fig. 5). In contrast, over the later age interval, only half increased, and almost 40% showed a decrease (Fig. 5), suggesting that the growth occurred by a different mechanism at the later age. Since regions of deposits with lower intensity (density) are areas of greater porosity, i.e., gaps in the mineral, this difference suggests that, in the earlier age interval, the growth mechanism is densification, a “filling in” of porous regions, whereas, in the older age interval, growth may be a combination of densification and/or addition of new, porous regions.

Histological analysis from aortic root sections

To obtain information about the population of deposits below the resolution of CT imaging, we performed histomorphometry of the aortic root from each mouse and analyzed the cross-sectional area, perimeter, as well as the perimeter-to-area ratio (PAR). The choice of these parameters is based on mathematical modeling with spherical and prolate spheroid approximations of hypothetical deposits and conversion from 3-D to 2-D representations (Fig. 6 A). This modeling shows that, for the same degree of total deposit 3-D volume, the total 2-D cross-sectional area of all deposits corresponds inversely with the degree of coalescence; a few large deposits have less cross-sectional area than many small deposits of the same volume. For instances where total deposit 3-D volume differs, a secondary parameter, Perimeter-to-Area Ratio (PAR), was found to correspond inversely with the degree of coalescence, as deposits of greatly differing size can have the same total surface area (Fig. 6 A-B). Lower PAR values correspond positively with coalescence in spherical and prolate spheroid approximated models. PAR is thus a pragmatic marker for deposit geometry, being inversely related to the degree of coalescence of deposits.

To acquire PAR values from the murine aortic root images, we used custom MATLAB software. We compared the PAR values for deposits within the range of 5 - 50 μm in diameter, between two groups of mice: one at 52 weeks and the other at 75 weeks of age. As shown in Fig. 6C, PAR decreased significantly with aging, suggesting a progression toward coalescence of smaller deposits into larger ones.

Effects of Western diet on morphological progression of vascular calcium deposits

To test the effects of the Western diet on morphological progression of the largest vascular calcium deposit in each mouse, we next compared mice that were on a control diet (standard; Group A, Mid to Pre; Fig. 3) with mice on a Western diet (Western; Group C, Post to Pre) in order to provide a similar time interval. As shown in Table III, over the 9-10 weeks of diet, the gain scores in the intensity parameters were not significantly different between the diet groups, but the median and 90th percentile intensity showed a trend toward an increase. As for the size features, the gain scores of surface area, volume and the diameter in the diet group were significantly greater than that of the control group (2.47-fold, 4-fold, 1.58-fold, respectively), suggesting that the diet promoted greater growth over this time period. In addition, the SA/V ratio decreased in both, but significantly more so in the diet group (0.67-fold), suggesting greater reduction of porosity. The shape parameters (elongation, flatness, and sphericity) were not affected significantly by Western diet. The texture features – autocorrelation (coarseness), cluster tendency, and non-uniformity - all increased significantly (3.87-fold, 2.8-fold, 2.23-fold), suggesting coarseness and heterogeneity.

Effects of high-intensity, progressive exercise on morphological progression of vascular calcium deposits

To test the effects of non-pharmacological intervention (high-intensity, progressive exercise) on calcium-deposit morphology, we compared the gain scores of each radiomic feature between the control (ad lib) and age-matched exercise groups (Groups D vs. C, Fig. 3). Results showed that all radiomic features exhibited a similar interval trend in the control as in the exercised group (Table IV).

In addition, to examine the broader population of deposits, we identified and counted spatially isolated calcium deposits by visual examination of 3-D reconstructed images of the thoracic cage. Results showed that the number of such calcium deposits increased significantly in the control group over the 9-wk period but not in the exercise group (Fig. 7).

Effects of pravastatin on morphological progression of vascular calcium deposits

To test the effects of pharmacological intervention on calcium deposit morphology, gain scores for each radiomic feature were compared between the pravastatin and age-matched control groups (Groups B vs. A; Fig. 3). All the radiomic features evaluated showed similar fold changes between the control and treatment groups (Table V).

However, the 3-D reconstruction and manual counting of spatially isolated deposits revealed that the number of such calcium deposits increased significantly in the control group over the 20-week period but not in the pravastatin group (Fig. 8A). Notably, mice on pravastatin had a significantly less increase in the number of deposits over the 20 weeks compared with the control group, and approximately 25% of pravastatin-treated mice had a decrease in the number of new calcium deposits compared with only 6% in controls (Fig. 8B).

DISCUSSION

To our knowledge, this study demonstrates for the first time the changes in radiomic features of cardiovascular calcification in mouse models with aging and standard interventions. We employed radiomic features of vascular calcium deposits in hyperlipidemic mice to assess features of calcification that cannot be determined from calcium scores from conventional CT or total calcium content alone. The CT scans included branches of the aorta and smaller blood vessels, but calcium deposits were not observed, though this may be attributable to the limits of resolution of the imaging as the functional transaxial (within-slice) resolution of the CT scans is approximately 220 μm. In brief, the findings show that aging had significant effects on intensity as well as size and texture of the largest deposits. Western diet also significantly affected the size and texture of the largest deposits, in a manner similar to that of aging. Interestingly, the radiomic features were not altered by the clinically relevant interventions including high-intensity, progressive exercise and pravastatin treatment.

We selected *a priori*, specific groups of radiomic features for this analysis, based on geometric and biomechanical considerations [27]. In general, intensity features are measures of x-ray attenuation, corresponding with mineral density, and density has been associated with stability [4]. Size features are generally expected to impact stability because *surface area* and *surface-area-to-volume ratio* (SA/V) indicate porosity which increases opportunity for compliance mismatch, localized stress concentration, and debonding at the mineral-tissue interface [7, 14]. Shape features are also determinants of stability [14, 28]. Higher interface stress occurs at sharp edges of sheet-like calcifications [29], whereas *sphericity* is associated with lower stress. Texture features are also expected to impact stability: *autocorrelation* is a measure of coarseness, while *cluster tendency, and non-uniformity* correspond with heterogeneity; the latter is generally associated with mechanical instability [14]. It is unclear whether autocorrelation, a measure of coarseness, favors mechanical stability or instability. Notably, the relationship of these features to stability depends greatly on the surface properties at the interface between tissue and calcification [27].

Consistent with prior clinical and preclinical studies, our analyses show consistent progression of calcification with age [22, 23, 30]. In addition, our findings suggest that the age-related progression occurs through some mechanisms that are expected to confer biomechanical instability and others that may confer stability. The radiomic features likely to be associated with stability are the increase in intensity features and the decrease in surface-area-to-volume ratio. The features likely to favor instability include decrease in sphericity and increase in cluster tendency and non-uniformity, which are related to heterogeneity, which is, in turn, associated with mechanical instability [27]. Overall, both stabilizing or destabilizing features occur with aging, and which one dominates over time is not yet known. At the population level, the incidence of acute cardiac events increases with age [31, 32], yet at the level of individual patients, it is also possible that plaque calcification and clinical picture may stabilize with age. The mouse ages in our study (55 - 75 wo) correspond roughly with human ages of 42 - 58 years [33]. In this range, plaque calcification may be shifting from porous to dense stages and clinical status from unstable to stable.

With respect to the Western diet, our radiomic analysis findings are consistent with prior studies [34-36], showing that a Western diet promotes vascular calcification. This diet caused changes in the radiomic features related to size and texture, and those changes were remarkably similar to those seen with aging, suggesting that a Western diet 'ages' the cardiovascular calcium morphology.

In the mice exposed to exercise and statin interventions, the calcification volume increased over time in all the groups to a similar degree, without significant differences, as seen in our previous analysis of calcium content [22, 23]. However, in the present study, the exercise intervention completely inhibited the significant increase in the number of spatially isolated calcium deposits observed over the 9-week period in the control group. This reduction in the number of new deposits suggests that exercise inhibits the development of small, nascent calcium deposits, evidently favoring contiguous growth of existing calcium deposits instead. As for the statin intervention, the number of new calcium deposits also increased in the control group, but significantly less in the pravastatin group. There were also some mice in the pravastatin group that had a net reduction in the number of calcifications. These findings suggest a tendency for contiguous growth as opposed to new deposits, which is consistent with the findings of Zhang et al. using ^{18}F-NaF PET/CT imaging in rabbits [37].

There are some limitations to this study. One is the level of microCT resolution, which we addressed in part by validating the radiomic CT results with histomorphometry. Additionally, our CT radiomic feature analysis characterized the morphology of only the largest deposits; this practical measure is a conventional approach to allow comparisons between groups given the large number of radiomic parameters and the large and unequal numbers of deposits [26]. However, it is possible to have a smaller deposit on the first scan overtake the progression and become the largest deposit on the second scan. In such a case, the change in the radiomic features may not be from the same deposit. However, in our sampling of a random 5% of scans, the largest deposit was the same one on the first and final scans.

Overall, these findings offer clues about whether interventions in humans may alter vascular calcium deposits in a manner that could explain the unexpected clinical observations of increased coronary calcification in response to therapeutic and preventive measures. The radiomic features of vascular calcification change significantly, with aging and diet, but not with high-intensity, progressive exercise regimen or pravastatin treatment. However, the latter interventions somewhat inhibit numbers of new calcium deposits. These changes may have implications for biomechanical stability of calcific atherosclerotic plaque. Human studies are needed to confirm whether radiomic features of calcification in coronaries (and other arteries) predict clinical outcomes. Such studies would require substantial computing power, but they would allow risk-stratification based on noninvasive imaging.

Supplementary Material

Refer to Web version on PubMed Central for supplementary material.

Acknowledgments:

The authors thank Dr. William Hsu, UCLA, for expert advice on deep learning segmentation and Dr. Amy Cummings, UCLA, for consultation on radiomic features.

Sources of Funding:

This work was funded by grants from the National Institutes of Health, Heart, Lung, and Blood Institute (HL137647, HL151391).

Glossary

***Apoe*$^{-/-}$**	Apolipoprotein E null
CT	Computed Tomography
^{18}F-NaF	Fluoride-18-labeled sodium fluoride
HU	Hounsfield Unit
PAR	Perimeter-to-area ratio
PET	Positron Emission Tomography
SA	Surface area
SA/V	Surface-area-to-volume ratio
V	Volume
wo	Week-old

References

[1]. Shioi A,Ikari Y. Plaque Calcification During Atherosclerosis Progression and Regression. J Atheroscler Thromb 2018; 25: 294–303. [PubMed: 29238011]

[2]. Shi X, Gao J, Lv Q, et al. Calcification in Atherosclerotic Plaque Vulnerability: Friend or Foe? Front Physiol 2020; 11: 56. [PubMed: 32116766]

[3]. Chen J, Budoff MJ, Reilly MP, et al. Coronary Artery Calcification and Risk of Cardiovascular Disease and Death Among Patients With Chronic Kidney Disease. JAMA Cardiol 2017; 2: 635–43. [PubMed: 28329057]

[4]. Criqui MH, Denenberg JO, Ix JH, et al. Calcium density of coronary artery plaque and risk of incident cardiovascular events. Jama 2014; 311: 271–8. [PubMed: 24247483]

[5]. Ehara S, Kobayashi Y, Yoshiyama M, et al. Spotty calcification typifies the culprit plaque in patients with acute myocardial infarction: an intravascular ultrasound study. Circulation 2004; 110: 3424–9. [PubMed: 15557374]

[6]. Jacobsen JC,Holstein-Rathlou NH. A life under pressure: circumferential stress in the microvascular wall. Basic Clin Pharmacol Toxicol 2012; 110: 26–34. [PubMed: 21917118]

[7]. Hoshino T, Chow LA, Hsu JJ, et al. Mechanical stress analysis of a rigid inclusion in distensible material: a model of atherosclerotic calcification and plaque vulnerability. Am J Physiol Heart Circ Physiol 2009; 297: H802–10. [PubMed: 19542489]

[8]. Leopold JA. Vascular calcification: an age-old problem of old age. Circulation 2013; 127: 2380–2. [PubMed: 23690467]

[9]. Saremi A, Bahn G,Reaven PD. Progression of vascular calcification is increased with statin use in the Veterans Affairs Diabetes Trial (VADT). Diabetes Care 2012; 35: 2390–2. [PubMed: 22875226]

[10]. Puri R, Nicholls SJ, Shao M, et al. Impact of statins on serial coronary calcification during atheroma progression and regression. J Am Coll Cardiol 2015; 65: 1273–82. [PubMed: 25835438]

[11]. Lemez S,Baker J. Do Elite Athletes Live Longer? A Systematic Review of Mortality and Longevity in Elite Athletes. Sports Med Open 2015; 1: 16. [PubMed: 26301178]

[12]. Morris JN,Crawford MD. Coronary heart disease and physical activity of work; evidence of a national necropsy survey. Br Med J 1958; 2: 1485–96. [PubMed: 13608027]

[13]. Aengevaeren VL, Mosterd A, Sharma S, et al. Exercise and Coronary Atherosclerosis: Observations, Explanations, Relevance, and Clinical Management. Circulation 2020; 141: 1338–50. [PubMed: 32310695]

[14]. Barrett HE, Van der Heiden K, Farrell E, Gijsen FJH,Akyildiz AC. Calcifications in atherosclerotic plaques and impact on plaque biomechanics. J Biomech 2019; 87: 1–12. [PubMed: 30904335]

[15]. Agatston AS, Janowitz WR, Hildner FJ, et al. Quantification of coronary artery calcium using ultrafast computed tomography. J Am Coll Cardiol 1990; 15: 827–32. [PubMed: 2407762]

[16]. Criqui MH, Forbang NI,Thomas IC. The Importance of Coronary Artery Calcium Density. JAMA Cardiol 2020; 5: 290–91. [PubMed: 31968048]

[17]. Cahalane RM, Barrett HE, O'Brien JM, et al. Relating the mechanical properties of atherosclerotic calcification to radiographic density: A nanoindentation approach. Acta Biomater 2018; 80: 228–36. [PubMed: 30218776]

[18]. Eslami P, Parmar C, Foldyna B, et al. Radiomics of Coronary Artery Calcium in the Framingham Heart Study. Radiol Cardiothorac Imaging 2020; 2: e190119. [PubMed: 32715301]

[19]. Maltbie E, Bhatt K, Paniagua B, et al. Asymmetric bias in user guided segmentations of brain structures. Neuroimage 2012; 59: 1315–23. [PubMed: 21889995]

[20]. Starmans MPA, van der Voort SR, Castillo Tovar JM, et al. In Zhou SK, Rueckert D,Fichtinger G, Eds. Handbook of Medical Image Computing and Computer Assisted Intervention Academic Press 2020; 429–56.

[21]. Moeskops P, Viergever MA, Mendrik AM, et al. Automatic Segmentation of MR Brain Images With a Convolutional Neural Network. IEEE Trans Med Imaging 2016; 35: 1252–61. [PubMed: 27046893]

[22]. Hsu JJ, Fong F, Patel R, et al. Changes in microarchitecture of atherosclerotic calcification assessed by (18)F-NaF PET and CT after a progressive exercise regimen in hyperlipidemic mice. J Nucl Cardiol 2021; 28: 2207–14. [PubMed: 31897996]

[23]. Xian JZ, Lu M, Fong F, et al. Statin Effects on Vascular Calcification: Microarchitectural Changes in Aortic Calcium Deposits in Aged Hyperlipidemic Mice. Arterioscler Thromb Vasc Biol 2021; 41: e185–e92. [PubMed: 33472400]

[24]. Ronneberger O, Fischer P,Brox T. U-net: Convolutional networks for biomedical image segmentation; 2015, Springer.

[25]. van Griethuysen JJM, Fedorov A, Parmar C, et al. Computational Radiomics System to Decode the Radiographic Phenotype. Cancer research 2017; 77: e104–e07. [PubMed: 29092951]

[26]. Papadopoulos A, Fotiadis DI,Likas A. Characterization of clustered microcalcifications in digitized mammograms using neural networks and support vector machines. Artif Intell Med 2005; 34: 141–50. [PubMed: 15894178]

[27]. Barrett HE, Cunnane EM, Kavanagh EG,Walsh MT. On the effect of calcification volume and configuration on the mechanical behaviour of carotid plaque tissue. J Mech Behav Biomed Mater 2016; 56: 45–56. [PubMed: 26655460]

[28]. Benitez J, Fontanarosa D, Wang J, et al. Evaluating the Impact of Calcification on Plaque Vulnerability from the Aspect of Mechanical Interaction Between Blood Flow and Artery Based on MRI. Ann Biomed Eng 2021; 49: 1169–82. [PubMed: 33079320]

[29]. Buffinton CM,Ebenstein DM. Effect of Calcification Modulus and Geometry on Stress in Models of Calcified Atherosclerotic Plaque. Cardiovascular Engineering and Technology 2014; 5: 244–60.

[30]. Paydary K, Revheim ME, Emamzadehfard S, et al. Quantitative thoracic aorta calcification assessment by (18)F-NaF PET/CT and its correlation with atherosclerotic cardiovascular disorders and increasing age. Eur Radiol 2021; 31: 785–94. [PubMed: 32870396]

[31]. Chapman AR, Adamson PD,Mills NL. Assessment and classification of patients with myocardial injury and infarction in clinical practice. Heart 2017; 103: 10–18. [PubMed: 27806987]

[32]. Newman AB, Naydeck BL, Sutton-Tyrrell K, et al. Coronary artery calcification in older adults to age 99: prevalence and risk factors. Circulation 2001; 104: 2679–84. [PubMed: 11723018]

[33]. Dutta S,Sengupta P. Men and mice: Relating their ages. Life Sci 2016; 152: 244–8. [PubMed: 26596563]

[34]. Aikawa E, Nahrendorf M, Figueiredo JL, et al. Osteogenesis associates with inflammation in early-stage atherosclerosis evaluated by molecular imaging in vivo. Circulation 2007; 116: 2841–50. [PubMed: 18040026]

[35]. Towler DA, Bidder M, Latifi T, Coleman T,Semenkovich CF. Diet-induced diabetes activates an osteogenic gene regulatory program in the aortas of low density lipoprotein receptor-deficient mice. J Biol Chem 1998; 273: 30427–34. [PubMed: 9804809]

[36]. Awan Z, Denis M, Bailey D, et al. The LDLR deficient mouse as a model for aortic calcification and quantification by micro-computed tomography. Atherosclerosis 2011; 219: 455–62. [PubMed: 22051553]

[37]. Zhang X, Chen X, Liang Z, et al. Atorvastatin Promotes Macrocalcification, But Not Microcalcification in Atherosclerotic Rabbits: An 18F-NaF PET/CT Study. Journal of cardiovascular pharmacology 2021; 78: 544–50. [PubMed: 34651601]

Highlights

- **Deep learning segmentation and CT radiomics** provided an objective and automated approach to assess changes in morphology of aortic calcium deposits in mice.
- **Aging** increased radiomic intensity (calcium mineral density), a potential plaque stabilizing effect; it also increased coarseness and relative surface area, while decreasing sphericity, all three potentially destabilizing effects.
- A **Western, high fat diet** increased calcification coarseness and relative surface area, which are potentially destabilizing effects.
- **Statin treatment** partially inhibited nascent calcification while **treadmill exercise** almost completely inhibited nascent calcification, thereby reducing surface area and potentially stabilizing plaque.

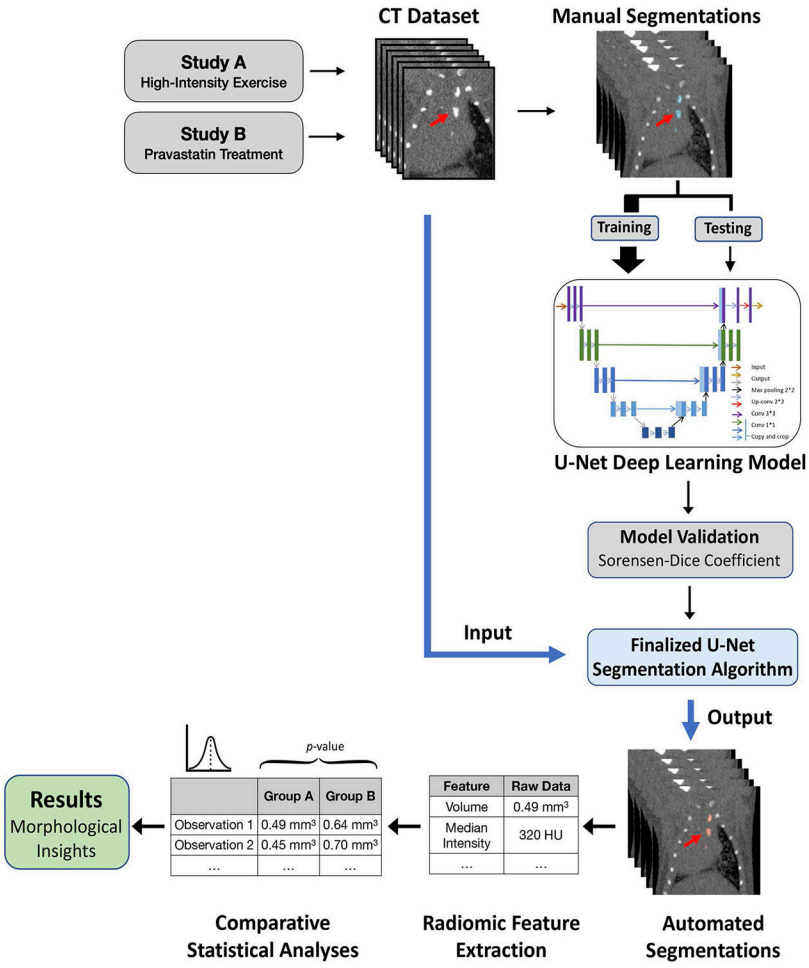

Figure 1. Flowchart of study methodology.

Data from both the high-intensity exercise and pravastatin studies were compiled to create a CT Dataset. CT scans were manually segmented to provide training and testing the U-Net Deep Learning Model (90:10 train-test split). After the U-Net model was trained, the model was validated, and all the CT scans were automatically segmented by the Finalized U-Net Segmentation Algorithm, radiomic features extracted using PyRadiomics, and statistical comparative analyses between the groups were performed. Red arrow indicates the largest aortic calcium deposit from a 3-D perspective. As a reference, the lengths of the deposits are approximately 2-3 mm. The dimensions of the images are approximately 20 mm x 20 mm.

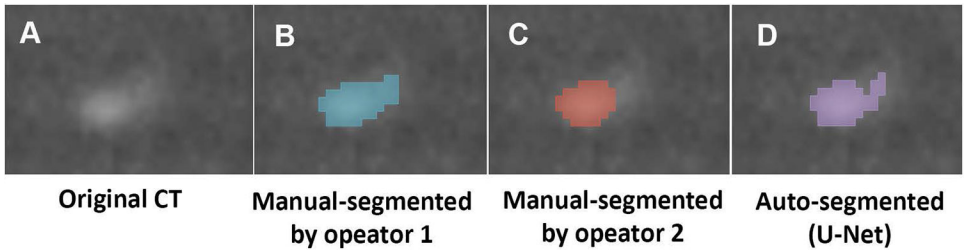

Figure 2. Example of segmentation validation of a small aortic calcification deposit.

Manual segmentations of an original CT image **(A)** by two different operators **(B and C)** and the automated segmentation produced by the fully trained U-Net deep learning algorithm **(D)**. As a reference, the length of the calcified deposit (blue-green area) in panel B is 2.2 mm. The dimensions of each of the four panels are 3.75 mm x 2.88 mm.

A

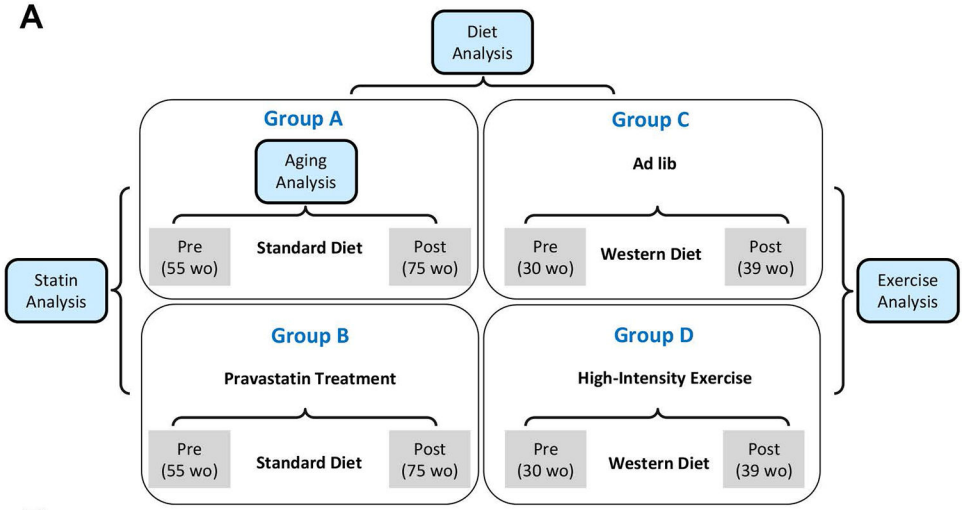

B

			Age (wo)		
Group	Diet	Intervention	Pre	Mid	Post
A	Standard	Control	55	65	75
B	Standard	Pravastatin	55		75
C	Western	Control	30		39
D	Western	Treadmill	30		39

Figure 3. Schematic of study group comparisons.

(A) Groups of mice analyzed from prior murine studies with different interventions. For aging analysis, Group A at age 55 weeks (n = 18) was compared to the same Group A mice at age 75 weeks (n = 18). For the diet analysis, the gain scores of Groups A and C were compared. For exercise analysis, the gain scores of Groups C and D were compared. For the statin analysis, the gain scores of Groups A and B were compared. **(B)** Analysis of age-related progression of calcification includes the third scan performed midway through the time interval at age 65 weeks of Group A.

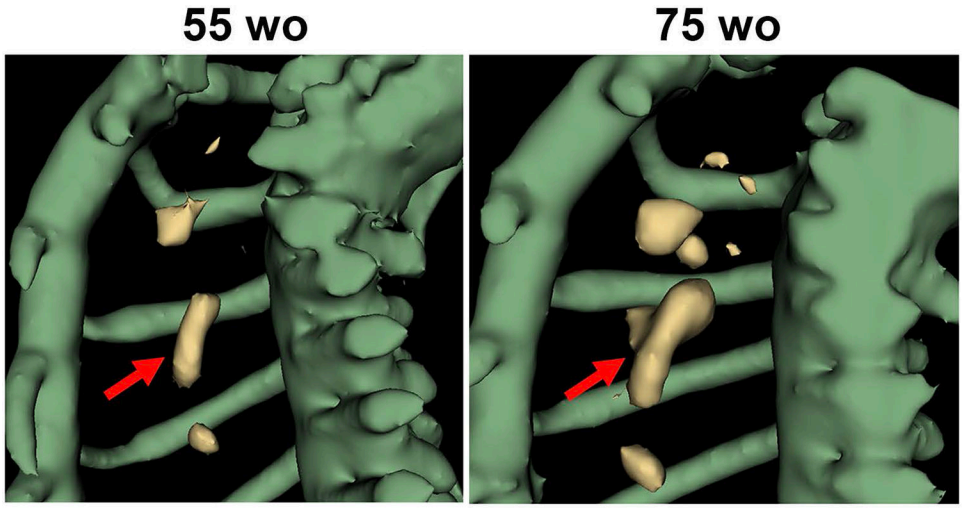

	Feature	55 wo	75 wo	Δ
Size	Surface Area (mm^2)	6.10	12.51	+ 6.41
	Volume (mm^3)	0.87	2.31	+ 1.44
	Maximum 3D Diameter (mm)	2.30	3.93	+ 0.64
	Surface Area/Volume Ratio	7.26	5.50	- 1.76
Shape	Elongation	0.42	0.70	+ 0.29
	Flatness	0.27	0.37	+ 0.09
	Sphericity	0.71	0.67	- 0.04
Texture	Uniformity	0.06	0.04	- 0.02
	Autocorrelation	173	370	+ 197
Intensity	10^{th} Percentile (HU)	323	360	+ 36
	Median (HU)	455	555	+ 100
	90^{th} Percentile (HU)	659	967	+ 307

Figure 4. 3-D rendering of morphologic changes in cardiovascular calcium deposits with aging.

3-D rendering of all aortic calcium deposits progression in the same mouse at 2 different time points: 55 and 75 weeks-old (wo). The lateral view of the upper thoracic region is shown with the left side of the ribcage removed for better visibility. (Also see 3-D animation of calcium deposits at 55, 65 and 75 wo in Supplemental Videos). Table describes the extracted radiomic features of the largest calcium deposit (red arrow) in the 55 wo and 75 wo scans.

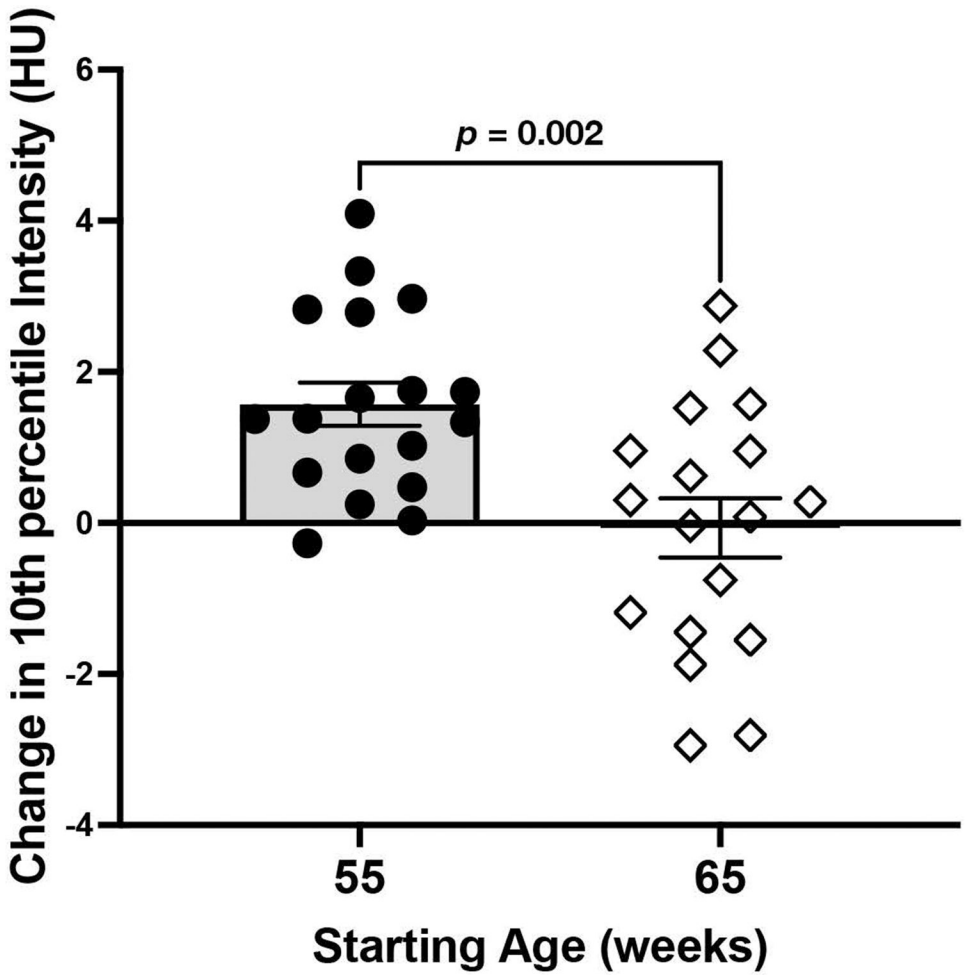

Figure 5. Effects of aging on small (10th percentile HU intensity) vascular calcium deposits.

Net change in 10th percentile intensity (Hounsfield units), in the same mice over two 10-week intervals, the first starting at 55 weeks of age (n = 18), and the second starting at 65 weeks of age (n = 18).

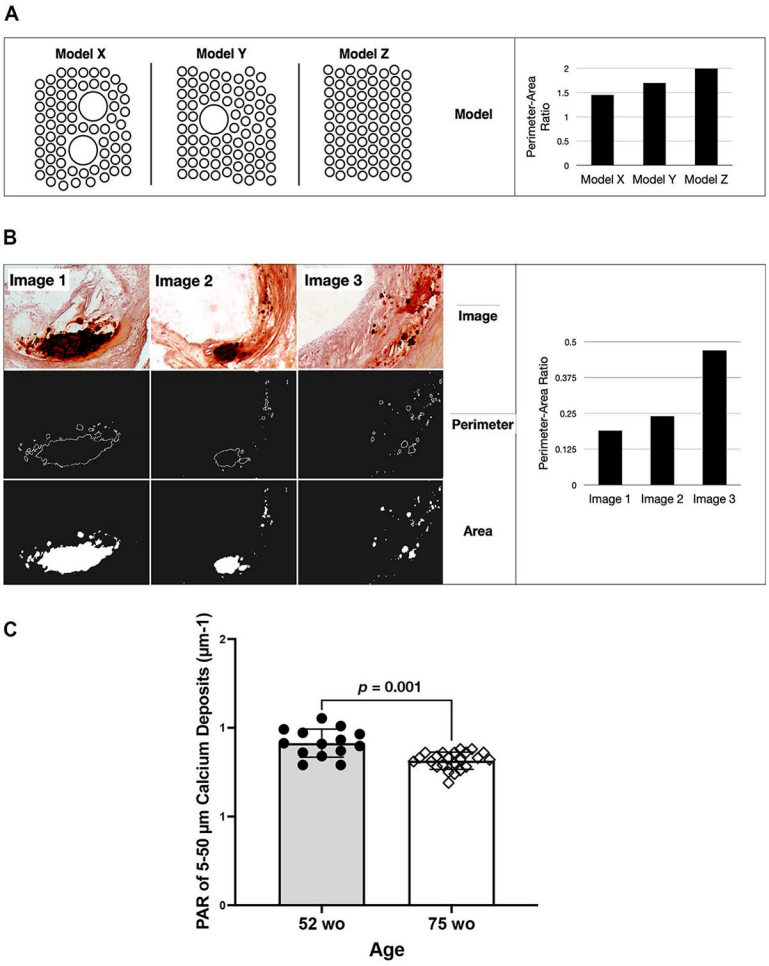

Figure 6. Perimeter-to-area ratio (PAR) determination of hypothetical deposits in mathematical models and murine aortic-root sections.

(**A, left**) 2-D depictions of three 3-D hypothetical models of spherical deposits, each model having the same total surface area but decreasing degrees of coalescence. **(A, right)** PAR of these 3 spherical models shown left. (**B, top left**) Images of 3 murine aortic-root histological sections with decreasing deposit sizes. (**B, middle left**) Perimeter of the respective calcium deposits calculated by custom MATLAB code. (**B, bottom left**) Cross-sectional area of the respective calcium deposits calculated by custom MATLAB code. (**B, right**) Perimeter-area ratio of the same 3 histological sections shown at left. **C.** Average PAR for all calcium deposits of diameter 5-50 μm in mice of age 52 (n = 14) vs. 75 weeks (n = 23). Measurements of perimeter and area of individual deposits were obtained using histological image analysis via custom MATLAB code.

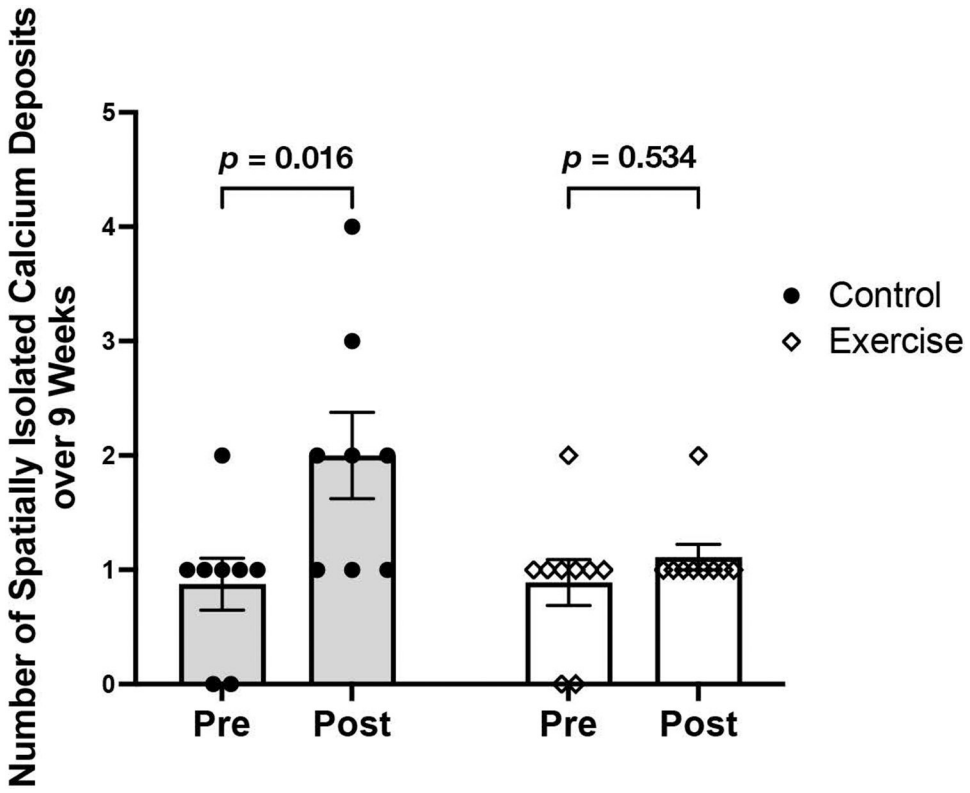

Figure 7. Effects of 9-week treadmill exercise on number of vascular calcium deposits.

The number of spatially isolated calcium deposits between the control (n = 8) and exercise groups (n = 9) over the course of the 9-week period.

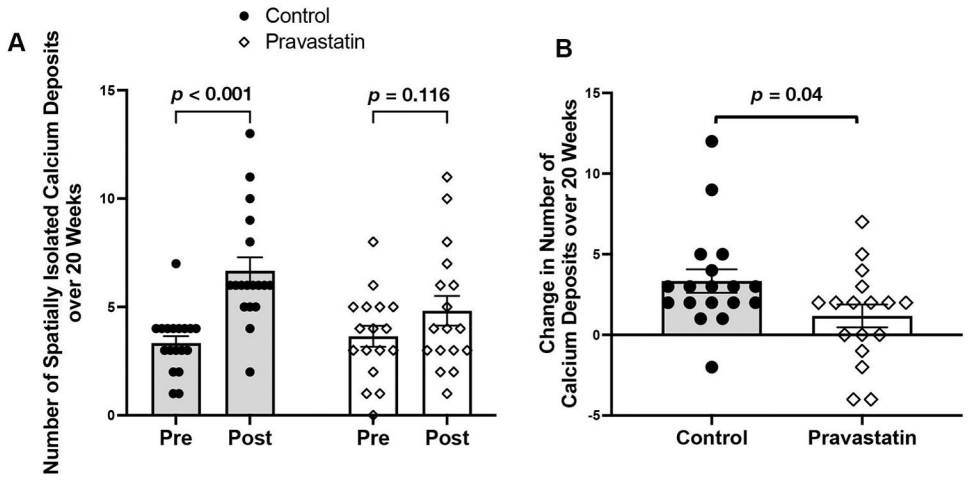

Figure 8. Effects of statin on the coalescence of vascular calcium deposits.

(A) The number of spatially isolated calcium deposits between the control (n = 18) and pravastatin (n= 18) groups over the course of the 20-week period. **(B)** The net change in the number of spatially isolated calcium deposits between the control and pravastatin-treated groups over the course of the 20-week period.

Table I.

Description of Radiomic Features

Radiomic Feature	Equation	Description
Elongation	$\sum \frac{\lambda_{minor}}{\lambda_{major}}$	λ_{minor} and λ_{major} are the lengths of the largest and second largest principal component axes. The values range between 1 (line) and 0 (maximally elongated).
Flatness	$\sum \frac{\lambda_{least}}{\lambda_{major}}$	λ_{major} and λ_{least} are the lengths of the largest and smallest principal components of axes. The values range between 1 (sphere) and 0 (flat).
Sphericity	$\frac{\sqrt[3]{36\pi V^2}}{A}$	A measure of the roundness of a calcium deposit relative to a sphere, where a value of 1 indicates a perfect sphere.
Autocorrelation	$\sum_{i=1}^{N_g} \sum_{j=1}^{N_g} p(i,j) i j$	A measure of the magnitude of the fineness and coarseness of texture.
Cluster Tendency	$\sum_{i=1}^{N_g} \sum_{j=1}^{N_g} [i + j - \mu_x(i) - \mu_y(j)]^2 p(i,j)$	A measure of groupings of voxels with similar gray level values from the 3-D gray level co-occurrence matrix.
Non-Uniformity (GLN)	$\frac{\sum_{i=1}^{N_g} [\sum_{j=1}^{N_r} p(i,j \mid \theta)]^2}{\sum_{i=1}^{N_g} \sum_{j=1}^{N_r} p(i,j \mid \theta)}$	A measure of the variability of gray level from the 3-D gray level run-length matrix.

TABLE II.

Effects of aging on radiomic features of vascular calcium deposits.

The absolute values between the Pre and Post time points in the control mice of the statin study were compared using paired *t*-tests.

	Feature	55 wo (Mean ± SEM) n = 18	75 wo (Mean ± SEM) n = 18	*p*-value
Intensity	10th Percentile (HU)	320 ± 5	335 ± 5	***0.004***
	Median (HU)	458 ± 17	509 ± 17	***0.002***
	90th Percentile (HU)	728 ± 56	908 ± 62	***0.002***
Size	Surface Area (mm^2)	3.66 ± 0.44	6.33 ± 0.69	***0.001***
	Volume (mm^3)	0.51 ± 0.08	1.01 ± 0.14	***0.001***
	Maximum 3D Diameter (mm)	1.55 ± 0.15	2.11 ± 0.16	***0.006***
	Surface Area/Volume Ratio	8.51 ± 0.51	6.95 ± 0.28	***<0.0001***
Shape	Elongation	0.66 ± 0.04	0.61 ± 0.04	0.110
	Flatness	0.50 ± 0.04	0.44 ± 0.03	0.074
	Sphericity	0.81 ± 0.02	0.76 ± 0.02	***0.039***
Texture	Autocorrelation	203 ± 40	358 ± 53	***<0.0001***
	Cluster Tendency	159 ± 44	337 ± 69	***0.002***
	Non-Uniformity	13.01 ± 1.23	20.34 ± 2.35	***0.010***

TABLE III.

Western diet effects on radiomic features of vascular calcium deposits.

Fold changes of Pre- to Mid-scans of the control mice (from the pravastatin study) were compared to those of Pre- to Post-scans of the control mice (from the exercise study) since these were similar time intervals.

	Feature	Control (fold ± SEM) n = 18	Western (fold ± SEM) n = 9	*p*-value
Intensity	10th Percentile	1.05 ± 0.01	1.13 ± 0.06	0.391
	Median	1.08 ± 0.03	1.23 ± 0.08	0.071
	90th Percentile	1.15 ± 0.06	1.36 ± 0.10	0.056
Size	Surface Area	1.53 ± 0.26	3.71 ± 1.25	***0.043***
	Volume	1.84 ± 0.43	7.15 ± 3.09	***0.007***
	Maximum 3D Diameter	1.25 ± 0.15	1.87 ± 0.35	***0.044***
	Surface Area/Volume Ratio	0.89 ± 0.02	0.63 ± 0.07	***<0.0001***
Shape	Elongation	1.03 ± 0.06	0.91 ± 0.09	0.320
	Flatness	0.99 ± 0.04	1.00 ± 0.12	0.925
	Sphericity	0.98 ± 0.01	1.07 ± 0.09	0.657
Texture	Autocorrelation	1.64 ± 0.26	6.16 ± 2.35	***0.025***
	Cluster Tendency	2.24 ± 0.64	6.23 ± 2.32	***0.005***
	Non-Uniformity	1.30 ± 0.12	2.85 ± 0.81	***0.005***

TABLE IV.

Exercise effects on radiomic features of vascular calcium deposits.

Fold changes of Pre- to Post-scans of the control mice to those of the exercise mice (from the exercise study).

	Feature	Control (Fold ± SEM) n = 9	Treadmill (Fold ± SEM) n = 9	*p*-value
Intensity	10th Percentile	1.13 ± 0.06	1.04 ± 0.10	0.748
	Median	1.23 ± 0.08	1.12 ± 0.13	0.473
	90th Percentile	1.36 ± 0.10	1.26 ± 0.17	0.329
Size	Surface Area	3.71 ± 1.25	3.59 ± 0.83	0.605
	Volume	7.15 ± 3.09	6.36 ± 2.02	0.730
	Maximum 3D Diameter	1.86 ± 0.35	1.86 ± 0.28	0.982
	Surface Area/Volume Ratio	0.63 ± 0.07	0.64 ± 0.07	0.897
Shape	Elongation	0.91 ± 0.09	0.85 ± 0.11	0.676
	Flatness	1.00 ± 0.12	1.31 ± 0.56	0.386
	Sphericity	1.07 ± 0.09	1.02 ± 0.09	0.307
Texture	Autocorrelation	6.16 ± 2.35	2.49 ± 0.67	0.438
	Cluster Tendency	6.23 ± 2.32	3.20 ± 1.08	0.265
	Non-Uniformity	2.85 ± 0.80	3.55 ± 1.01	0.546

TABLE V.

Pravastatin effects on radiomic features of vascular calcium deposits.

Fold changes of Pre- to Post-scans of the control mice to those of the pravastatin mice (from the pravastatin study).

	Feature	Control (Fold ± SEM) n = 18	Pravastatin (Fold ± SEM) n = 16	*p*-value
Intensity	10th Percentile	1.05 ± 0.01	1.05 ± 0.01	0.490
	Median	1.12 ± 0.03	1.17 ± 0.03	0.160
	90th Percentile	1.29 ± 0.08	1.32 ± 0.05	0.206
Size	Surface Area	2.23 ± 0.47	1.70 ± 0.12	0.871
	Volume	2.94 ± 0.76	2.06 ± 0.17	0.511
	Maximum 3D Diameter	1.53 ± 0.18	1.30 ± 0.07	0.779
	Surface Area/Volume Ratio	0.84 ± 0.03	0.83 ± 0.03	0.397
Shape	Elongation	0.97 ± 0.16	1.16 ± 0.12	0.184
	Flatness	0.92 ± 0.06	1.08 ± 0.14	0.689
	Sphericity	0.94 ± 0.03	0.97 ± 0.03	0.676
Texture	Autocorrelation	2.19 ± 0.31	2.20 ± 0.26	0.478
	Cluster Tendency	3.58 ± 0.95	3.05 ± 0.42	0.248
	Non-Uniformity	1.88 ± 0.44	1.41 ± 0.12	0.740